

Hydrothermal metalliferous sediments in Red Sea deeps: Formation, characterization and properties

M. Clara Modenesi^{*}, J. Carlos Santamarina

King Abdullah University of Science and Technology KAUST, Thuwal 23955-6900, Saudi Arabia

ARTICLE INFO

Keywords:

Hydrothermal sediments
Stiffness
Strength
Consolidation
Deep-sea mining
Soil Classification

ABSTRACT

Sediment accumulations within the Red Sea central deeps have unique genesis and properties. We piece together available information to understand their geological setting and formation history, and conduct an extensive sediment characterization study to assess their geotechnical properties in order to anticipate engineering/mining implications. The various sediment columns reflect slow-rate background sedimentation (biogenic and detrital particles – Valdivia deep) and hydrothermal metalliferous sediments that nucleate and grow within the overlying brine pools (primarily in the Atlantis II, as well as in the Wando deep, and to a lesser extent in Discovery deep). All sediments are fine-grained silt and clay-size particles; smaller particles tend to have higher specific gravity and define the metalliferous content. Hydrothermal sediments exhibit extreme properties when compared to sediments worldwide: they have uncharacteristically large maximum void ratio and compressibility, and their self-compaction is very different from background Red Sea sediments. Their unique self-compaction trends have a strong effect on remote acoustic characterization and sampling, and must be carefully accounted for during field studies and resource assessment. Three distinct properties of hydrothermal metalliferous sediments are relevant for separation and enrichment: high specific surface area, high specific gravity, and ferromagnetic signature. Small grains and low-density flocs have low terminal Stokes' velocities and their residency times may be extended in convective stratified brine pools; this observation affects the environmental analysis of mining operations and tailings disposal.

1. Introduction

The Red Sea rifting started approximately 30 Myr ago, between the late Oligocene to early Miocene, as evidenced by igneous activity in the region (Coleman, 1993). Seafloor spreading began 12 Myr ago (Izzeldin, 1987). Concurrently, evaporite sequences deposited during the rift evolution, particularly during the Miocene (Orszag-Sperber et al., 1998). Then, Pliocene to recent sediments covered the massive layered salts and anhydrite accumulations (Stoffers and Ross, 1974). Seafloor spreading creates the space for salt flows to creep down the rift flanks and reshape the bathymetry; however, seafloor spreading is faster than salt creep in central latitudes, leading to the formation of the central trough along the Red Sea (Mitchell et al., 2010; Augustin et al., 2014).

Salinity and temperature anomalies detected in the late 1940s motivated early research cruises to study features in the central Red Sea areas (mentioned in Miller, 1964; Charnock, 1964). The Discovery brine pool identified in September 1964 showed the presence of hot brines within deeps (Swallow and Crease, 1965). Soon after, explorations

identified the presence of a hot and stratified brine pool overlying metalliferous sediments in the Atlantis II deep (Miller et al., 1966). These findings motivated extensive studies of the Atlantis II deposits and brine pool and subsequent explorations to other regions along the central trough (Degens and Ross, 1969). The Saudi-Sudanese Red Sea Commission evaluated the economic potential of the Atlantis II deep and a pre-pilot mining test took place in 1979 (Mustafa and Amann, 1980). The Commission concluded that the Atlantis II deep contains approximately 90 million tons of dry-salt-free materials enriched in Zn, Cu, Ag, Au and Co (Guney et al., 1988). However, a decrease in the price of metals in the early 1980s delayed deep-sea mining activities in the Red Sea. Renewed interest commenced in 2010 when the Sudanese and Saudi governments granted a 30-year mining license to Manafa International Trade Company (Saudi Arabia) and Diamondfields International Ltd. (Canada) for the Atlantis II project.

Engineering and environmental challenges associated with deep-sea mining will determine our ability to meet future demands for mineral resources. This study focuses on sediment accumulations in the Atlantis II and the neighboring deeps Discovery, Valdivia and Wando. We bring

^{*} Corresponding author.

E-mail address: maria.modenesi@kaust.edu.sa (M.C. Modenesi).

Notation

A [m ²]	Deposit areal extent
c_b [kg.m ⁻³]	Ionic concentration
C_C []	Compression index
c_{metal} [kg.kg ⁻¹]	Metal concentration
d [μm]	Particle size: d_{50} mean grain size
e	Void ratio: e_z at depth z ; e_{1kPa} at 1 kPa; e_L & e_H asymptotic values at low and high effective stress; 'in-situ': maximum in-situ
g [m.s ⁻²]	Gravitational acceleration
G_S []	Specific gravity
G_{max} [kPa]	Small strain shear modulus
H [m]	Deposit height
h [m]	Fall height
H_b [m]	Convective layer thickness
LL [%]	Liquid limit
M_{metal} [kg]	Metal mass
M_{sed} [kg]	Sediment mass
n []	Porosity
r [m]	Gravity corer radius
r_f [μm]	Final particle radius
S_S [m ² .g ⁻¹]	Specific surface area

S_U [kPa]	Sediment undrained shear strength
v_c [m.s ⁻¹]	Convection velocity
V_S [m.s ⁻¹]	Shear wave velocity
W_B [N]	Buoyant weight
W_w [%]	Water content
z [m]	Depth
α [m.s ⁻¹]	Shear wave velocity at 1 kPa vertical effective stress
α_T [1.°C ⁻¹]	Thermal expansion coefficient
β -exponent	Shear wave velocity sensitivity to effective stress
ΔT [°C]	Thermal jump across the boundary
ϕ [°]	Friction angle
γ_r [%]	Shear strain
η -exponent	Void ratio sensitivity to effective stress
λ [m]	Convective-belt characteristic thickness
μ [Pa.s]	Dynamic viscosity
μ_r []	Relative magnetic permeability
ρ [g.cm ⁻³]	Density: ρ_p particle; ρ_{min} mineral; ρ_{ws} wet sediment; ρ_b brine; ρ_w water; ρ_{metal} metal
σ' [kPa]	Effective stress: σ'_z vertical at depth z ; σ'_c characteristic; σ'_A equivalent due to electrical attraction; σ'_m mean (polarization plane); σ'_{zav} average along core; σ'_{ztip} at corer tip

together geology and geotechnical engineering to understand the geological setting and formation history, to characterize the sediment properties and to anticipate engineering/mining implications. First, we compile published results to piece together the sediment formation history in the central trough of the Red Sea. Then, we present a comprehensive sediment characterization study in view of potential deep-sea mining operations.

2. Atlantis II: sediment formation

Deep-sea background sediments in the central Red Sea include biogenic carbonates – mostly high and low-magnesium calcite and subordinately aragonite (Gevirtz and Friedman, 1966; Stoffers and Ross, 1974), and aeolian particles transported during frequent dust storms primarily composed of silt-sized quartz and feldspar (Engelbrecht et al., 2017).

Typical seawaters throughout the bottom of the Red Sea have an average 40‰ salinity and a temperature of 22 °C. Localized hydrothermal circulation through Miocene evaporites and underlying basaltic rocks produces high salinity metal-enriched fluids which often accumulate in deeps. Convection couples with thermal and chemical diffusion to cause brine stratification into multiple layers with sharp physicochemical boundaries (Turner, 1969). The chemical composition of the various layers creates a unique environment for mineral formation and precipitation resulting in the accumulation of hydrothermal metalliferous sediments within some deeps (Backer and Schoell, 1972; Bignell et al., 1976).

The Atlantis II deep sits on the rift axis in the central Red Sea and covers nearly 60 km² at a water depth of more than 2000 m (Fig. 1). Salt flows and NW-striking faults bound the deep (Augustin et al., 2016). Minor adjoining deeps sit to the west of the Atlantis II and include the Wando Deep, Valdivia Deep, and the Discovery Deep connected through the Chain deeps (Fig. 1).

The Atlantis II is the largest deep in the Red Sea and it is filled with a stratified brine pool. The lower convective layer is ~119 m thick (water depth ~2051 to ~2170 mbsl in the Atlantis II SW area) and has ~270‰ salinity at 69 °C. The sediment column in the Atlantis II deep records the formation history and shows pronounced changes in the last 28 ky (e.g., Bäcker and Richter, 1973; Hackett and Bischoff, 1973; Anschutz and

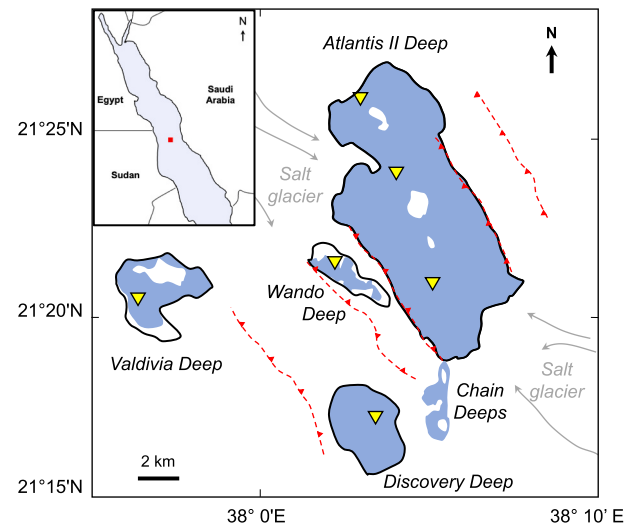


Fig. 1. Central Red Sea deeps: Atlantis II, Wando, Discovery and Valdivia. Yellow markers: gravity cores. Brine flooding surfaces (blue): Atlantis II, Wando and Discovery deeps at 1995 mbsl; Valdivia deep at 1524 mbsl. Dotted lines: normal faults. Arrows: salt glaciers. (For interpretation of the references to color in this figure legend, the reader is referred to the web version of this article.)

Blanc, 1995a). Early sediment accumulation rates resemble normal deposition conditions (~2.5 mm/yr) with sporadic hydrothermal input during the first ~15 ky. High-accumulation rates (10–12 mm/yr) associated with hydrothermal activity dominate the sediment column thereafter (Shanks and Bischoff, 1980).

The hydrothermal sediments in the Atlantis II include sulfides, oxyhydroxides, clays, carbonates, sulfates and amorphous phases (Bischoff, 1969; Bäcker and Richter, 1973; Bignell et al., 1976). Sulfides, such as sphalerite and chalcocopyrite are the most relevant mineral ores; however, non-sulfide phases such as Si-Fe-oxyhydroxides and authigenic clays incorporate metals by adsorption during diagenesis and can be relevant as well (Laurila et al., 2014; Laurila et al., 2015). Stable isotopes indicate

either hydrothermal input or bio-mediated sulfate reduction as potential sulfur sources (Shanks and Bischoff, 1980). The present lower convective brine layer (water depth ~ 2051 to ~2170 mbsl in the SW-basin) contains dissolved metals but lacks hydrogen sulfide; these characteristics suggest that the hydrothermal sulfides precipitate by cooling within the lower convective layer in close proximity to the vents (Shanks III and Bischoff, 1977). Sulfate-reducing and methane-oxidizing bacteria identified in the more recent Atlantis II sulfur-enriched sediments in the upper 3.5 m of the sediment column hint to the role of microbial activity on the sulfur cycle (Siam et al., 2012).

The Fe-Mn oxyhydroxides form by oxidation of Fe⁺² and Mn⁺² within the upper oxidizing layers (water depth ~ 2000 to <~2055 mbsl for Fe, and water depth < ~2010 for Mn; Hartmann, 1985, Butuzova et al., 1990). Mn-oxyhydroxides settle along the deep's flanks where oxidizing conditions prevail but dissolve in the lower brine at present conditions. Fe-oxyhydroxides accumulate in the sediment column primarily as amorphous phases; goethite and hematite are common crystalline phases (Butuzova et al., 1990; Taitel-Goldman and Singer, 2001). Amorphous Fe-Si particles abound in the recent deposits and may form within the lower brine layer and at the sediment interface; diagenesis later transforms these particles into crystalline clay phases (Anschutz and Blanc, 1995b; Taitel-Goldman and Singer, 2002).

The unique regional geology setting, sediment formation processes and depositional environment anticipate distinctive geomechanical properties with important implications to potential mining operations. The sediment characteristics and properties are investigated next.

3. Characterization studies – protocols and results

Research cruises aboard KAUST's RV Thuwal investigated the Atlantis II, Discovery, Wando, and Valdivia deeps in February and September 2019. We collected gravity cores from the upper part of the sedimentary column (sampling locations in Table 1). The gravity corer is a 3-m-long stainless-steel pipe (130 kg in air) coupled to an additional 80 kg mass (in air). A PVC liner (internal diameter *ID* = 86 mm) is placed inside and held by the core catcher and the cutting shoe. The gravity corer is lowered at a controlled velocity. Recovered sediments are stored inside the plastic liner. We obtained 100% core recovery in the soft sediments of the Atlantis II and Discovery deeps, but partial recovery in Wando and Valdivia deeps where coarse-grained layers hindered penetration (in fact, gravel-size grains were retained at the core catcher). The cores were stored in a cold room at 4 °C and later subjected to a comprehensive laboratory study. This section describes test protocols and summarizes sediment properties (Tables 2 and 3).

3.1. Sediment structure and variability (CT-scan and photographs)

We inspected the gravity cores using X-Ray CT imaging (CoreTOM, XRE, 125 µm voxel size); then, we split the cores and photographed the fresh surfaces. Fig. 2 shows representative pictures next to the vertical slices from the 3D tomograms. X-Ray and optical images provide evidence of vertical variability in Atlantis II and Wando sediments with clear compositional changes evidenced by color variations (photographs) and X-ray absorption (gray level in CT-slices). In contrast, Valdivia deep deposits show slight changes and Discovery deep deposits

appear relatively homogeneous. Soft seafloor sediments are susceptible to sampling effects, including stress changes, the deflection of laminates in the direction of core insertion and the formation of exsolution bubbles (the latter two observed in CT-scan images - Fig. 2; see also Blouin et al., 2019 and Dai and Santamarina, 2014).

3.2. Sample preparation

The salinities within the water column vary from seawater to brines (40‰ to 270‰). Test protocols and data analyses consider the influence of dissolved salts on fine-grained sediments: high ionic concentration collapses the double-layer and favors particle aggregation, while excess salts precipitate during drying and affect the determination of the dry mineral mass. Several standardized test procedures require the use of deionized water, such as hydrometer, pycnometer and specific surface tests; in these cases, we suspended sediments in de-ionized water to remove excess salts.

3.3. Index properties

Samples gathered from homogenous layers along each core capture the various sediment formations, properties, and behavior.

Mineralogy and Elemental Composition. We observed grains using a scanning electron microscope SEM (Teneo FEI, sputter coated with Ir) complemented with energy dispersive spectroscopy EDS to determine the elemental composition. Complimentary X-ray diffraction measurements XRD did not provide discriminating results due to the complex mineralogy found in these specimens. The quantification of prevalent elements involved ICP-OES (Inductively Coupled Plasma Atomic Emission Spectroscopy, Agilent 5110). The sample preparation included oven-drying specimens at 105 °C, pulverization using an agate mortar followed by microwave digestion in an HNO₃-HCl-HF solution and further dilution with deionized water. A blank reagent, a quality control solution and a sediment sample spiked with a known concentration solution were also included in the digestion batch. The test procedure consisted of routine blanks and sample duplicates. We assumed that Na was present only as halite to correct concentrations for dry-salt-free material. Table 2 summarizes element quantifications for dry-salt-free sediment.

Representative SEM images in Figs. 3 and 4 highlight the diverse mineralogy, particle shapes and sizes observed in sediments collected from the deeps. Mineralogy (Figs. 3 and 4), elemental composition (Table 2) and layering information (Fig. 2) point to distinct features in the several deeps:

- Atlantis II deep: there is a predominant hydrothermal influence with abundant clays, sulfides such as sphalerite, Fe-Mn carbonates, oxides, and Ca and Ba sulfates in the recent/upper accumulations; biogenic constituents are present as minor components and often show chemical degradation (see also Laurila et al., 2015).
- Wando deep: sediments consist of clays, Fe and Mn-rich oxides, Mn-rich carbonates, Ba-sulfates, and minor biogenic carbonates and detrital particles. Fe and Mn minerals suggest some influence from the adjacent Atlantis II deep. Alternate light-colored layers capture

Table 1

Coordinates for recovered gravity cores. Depths below sea level based on site bathymetry.

Location	Coordinates		Water Depth [mbsl]	Recovered Length [m]	Structure
Atlantis II Deep (SW)	21° 20' 37.16" N	38° 4' 48.94" E	2140	3.0	Layered
Atlantis II Deep (North Passage)	21° 23' 57.03" N	38° 3' 45.04" E	2040	2.7	Layered
Atlantis II Deep (NE)	21° 25' 25.26" N	38° 3' 15.72" E	1985	3.0	Layered
Wando Deep	21° 21' 33.72" N	38° 2' 7.74" E	1915	2.1	Layered
Discovery Deep	21° 17' 17.52" N	38° 3' 33.90" E	2068	3.0	Homogen.
Valdivia Deep	21° 20' 14.82" N	37° 56' 52.14" E	1528	1.5	Layered

Table 2

Elemental composition. Depths indicate sample location from the top of the core. Results obtained from ICP-OES measurements for the different tested samples. Values are corrected for NaCl concentration (d.l.: measurement at or below the instrument detection limit; n.d.: not determined).

Sample information		Geochemistry									
Deep	Depth	Ag	Al	Ca	Co	Cu	Fe	Mg	Mn	Pb	Zn
	[m]	[ppm]	[%]	[%]	[ppm]	[%]	[%]	[%]	[%]	[ppm]	[%]
Atlantis II (SW Basin)	0–0.3	97	0.2	1.4	232	0.8	33.9	0.21	0.3	1142	5.0
Atlantis II (SW Basin)	2.2–2.4	166	0.3	0.5	157	1	45.2	0.17	0.4	2730	10
Atlantis II (N-Passage)	0–0.4	21	0.3	1.3	70	0.2	48.5	0.20	0.2	783	0.8
Atlantis II (N-Passage) dup.	0–0.4	21	0.3	1.3	69	0.2	n.d.	0.20	0.2	764	0.7
Atlantis II (N-Passage)	1.8–2	39	0.2	1.3	127	0.3	49.9	0.26	0.5	646	2.3
Atlantis II (NE Basin)	0–0.75	15	0.2	1.9	55	0.1	45.9	0.27	0.2	363	0.6
Wando	0–0.3	21	284 ppm	2.1	83	510 ppm	8.3	0.66	32.5	106	0.6
Discovery	0–0.3	dl	205 ppm	3.6	23	170 ppm	7.4	0.83	3.1	59	879 ppm
Valdivia	0–0.3	dl	295 ppm	4.9	17	56 ppm	3.5	0.90	0.2	dl	162 ppm

normal Red Sea background sedimentation between dark-colored layers that record cycles of high hydrothermal activity (Fig. 2).

- Discovery deep: sediments contain biogenic carbonates (e.g., coccoliths, foraminifera), Ca-Mg carbonates such as dolomite, clays and a minor fraction of Fe-oxides. The abundant biogenic carbonates and hydrothermal minerals in the Discovery deep point to a mixed normal Red Sea background sedimentation and hydrothermal origin.
- Valdivia deep: sediments are predominantly biogenic carbonates and Ca-Mg carbonates such as dolomite, silicates of possibly detrital origin and pyrite (see also Backer and Schoell, 1972; Pierret et al., 2000). The Valdivia deep deposits correspond to normal Red Sea sedimentation with minor hydrothermal influence.

The Discovery and Valdivia deep accumulations show no significant changes in the recent history (e.g., few thousand years based on upper sediment data). The mining significance of surface sediments in the Wando deep is considerably lower than in the Atlantis II deep. Sediments in the Discovery and Valdivia deeps do not contain significant amounts of mining metals.

Specific gravity. We obtained the sediment specific gravity G_S using the pycnometer method (ASTM International, 2014). Measurements show a wide range of specific gravities from $G_S = 2.76$ to $G_S = 3.58$ (Table 3). Measured values are mass-averages of the different minerals present in specimens, from clays (montmorillonite $G_S \approx 2.5$) and calcite ($G_S \approx 2.83$) to heavier minerals such as sulfides, Fe-Mn oxides, Fe-carbonates and Ba-sulfates (e.g., sphalerite $G_S = 4.00$, siderite $G_S = 3.96$, magnetite $G_S = 5.18$, barite $G_S = 4.48$). Overall, higher specific gravity grains define the metalliferous content (Fig. 5).

Grain size distribution. Sediments in the four deeps are fine-grained, silt-to-clay size, with a fines content passing sieve #200 between 80% and 100%. We determined the particle size distribution of the fines fraction using the sedimentation-hydrometer test (fraction passing the sieve #200; sodium hexametaphosphate dispersant; ASTM International, 2017). Results indicate that 15% to 44% of the sediment mass is finer than 2 μm . The mean grain size ranges between $d_{50} = 1 \mu\text{m}$ and $d_{50} = 12 \mu\text{m}$ (Fig. 6). Data points in Fig. 6 are color-coded according to average specific gravity: results show a trend towards smaller particle size for higher specific gravity grains.

Specific surface area. We used colorimetry with crystal violet dye to measure the specific surface area S_S [$\text{m}^2 \cdot \text{g}^{-1}$] of washed sediments passing through sieve #200 (Salva Ramirez and Santamarina, 2021). The specific surface area for all sediments recovered from the four deeps varies between $S_S = 55 \text{ m}^2 \cdot \text{g}^{-1}$ and $S_S = 177 \text{ m}^2 \cdot \text{g}^{-1}$ (Table 3). Typical pelagic Red Sea sediments have specific surface areas that range from $S_S \sim 20 \text{ m}^2 \cdot \text{g}^{-1}$ to $S_S \sim 55 \text{ m}^2 \cdot \text{g}^{-1}$ (For reference: kaolinite $S_S = 10\text{--}20 \text{ m}^2 \cdot \text{g}^{-1}$, illite $S_S = 80\text{--}100 \text{ m}^2 \cdot \text{g}^{-1}$, and montmorillonite $S_S = 400\text{--}800 \text{ m}^2 \cdot \text{g}^{-1}$. Santamarina et al., 2002). The high specific surface areas of the sediments from these deeps correspond to small grain sizes between 12 nm and 40 nm (assuming $\rho_p = 2.7 \text{ g} \cdot \text{cm}^{-3}$ – Note: the larger mean particle size determined from hydrometer data hints to aggregation).

This result highlights the dominant role of the finest particles on the sediment specific surface area.

Fines: Liquid Limit and Water Content. Liquid limit LL [%] determinations followed the fall cone test procedure using the in-situ pore fluid to capture the effects of brine on sediment plasticity (BS 1377–2, BSI, 1990; Jang and Santamarina, 2016; all values are corrected for salt precipitation). Results in Fig. 7 show a wide range of liquid limits, from $LL = 80\%$ to $LL = 328\%$. The highest values correspond to Atlantis II deep sediments and the lowest to Valdivia deep deposits. The “in-situ” water content W_w was determined once onshore by oven-drying at 105 °C until constant mass. The values were corrected for salt precipitation, assuming that the sediment is saturated with a NaCl brine pore fluid that has equal ionic concentrations to the brine immediately above the sediment (e.g., for the Atlantis II, the lower-most brine layer has salinities of 270‰). The in-situ water content W_w [%] is considerably above liquid limits in all cases (measured for different stratigraphic layers), and it exceeds twice the liquid in Atlantis II and Wando deep sediments. Clearly, these are “sensitive” sediments (where sensitivity is defined as the ratio between the undisturbed and the remolded undrained shear strength). In fact, these are not uncommon characteristics: extra-sensitive clays can exhibit sensitivities above 100. Within the framework of marine sediments, we assume a soil exists as soon as it forms a granular skeleton and allows for shear wave propagation.

Hydrothermal sediments exhibit high liquid limits and high plasticity compared to typical Red Sea sediments (e.g., pelagic carbonates and detrital silicates), and should be sensitive to changes in pore fluid chemistry. All specimens fall under the category of fines-controlled mechanical and hydraulic properties in the Revised Soil Classification System (Park and Santamarina, 2017).

Maximum in-situ void ratio. The sedimentation of low-solids suspensions emulates fabric formation in ‘newly formed’ deposits. We suspended sediments that have not been previously dried in a NaCl solution with equal ionic concentration to the in-situ brines and let them rest in 50 ml transparent plastic tubes until the upper solution was clear. The final sediment volume V_T [ml] and the sediment dry mass M_S [g] corrected for salt precipitation allowed us to compute the ‘maximum void ratio’. Values span two orders of magnitude, from $e_{\text{in-situ}} = 2$ to 127 (Table 3). The highest void ratios correspond to Atlantis II specimens. High void ratios imply extremely light and soft upper layers, with wet densities as low as $\rho_{ws} = 1206 \text{ kg} \cdot \text{m}^{-3}$, quite similar to the brines in the water column immediately above the sediment $\rho_b = 1187 \text{ kg} \cdot \text{m}^{-3}$ (for 270‰ salinity and 69 °C temperature at 20 MPa of pressure; empirical equation in Mavko et al., 2009).

Magnetic Properties. A magnetic field readily separates magnetic particles from sediment suspensions prepared with a dispersant to minimize particle aggregation (5 g of sodium hexametaphosphate). Fig. 8a shows SEM images of magnetically separated Fe-oxides from Atlantis II deep specimens. These ferromagnetic particles affect the overall magnetic permeability of hydrothermal sediments. We measured the magnetic permeability at 300 K (27 °C) using a SQUID-VSM

Table 3
Sediment Properties. Depths indicate sample location from the top of the core.

Sample Information	Index Properties and Classification										Geomechanical									
	Depth [m]	G _s [g/cm ³]	d ₅₀ [μm]	Pass #200 [%]	S _s [m ² /g]	LL [%]	W _w [%]	e _{in-situ} []	RSCS	Magnet. μ _r []	Consolidation			Shear wave velocity				Simple shear		
Deep										C _c *	C _c **	e _L []	e _H []	σ _c ' [kPa]	σ _c ^A [kPa]	α-factor [m/s]	β-expon. []	φ [°]	G _{max} [kPa]	γ _r [%]
Atlantis II (SW Basin)	0-0.3	3.44	8	92	104	-	86	F(F)	1.0024	4.30	5.87	22.0	0.4	60	3.3	5.0	0.52	19.3	8.0	2.3
Atlantis II (SW Basin)	2.2-2.4	3.41	9	80	99	197	495	F(F)	1.0042	3.62	5.44	21.5	0.3	120	3.5	6.5	0.55	20.5	8.3	2.1
Atlantis II (N-Passage)	0-0.4	3.58	2	98	94	-	-	F(F)	1.0056	0.93	1.48	7.8	1.7	190	2.0	10.5	0.53	-	-	-
Atlantis II (N-Passage)	1.8-2	3.42	1	100	142	328	782	F(F)	1.0044	6.99	8.23	34.0	3.6	28	2.5	5.3	0.59	19.5	5.1	4.6
Atlantis II (NE Basin)	0-0.75	3.45	2	98	177	-	77	F(F)	1.0025	4.35	6.00	23.1	0.7	65	2.2	5.5	0.53	21.0	4.5	5.2
Wando	0-0.3	3.33	6	84	-	224	655	F(F)	1.0012	1.95	3.22	15.5	1.0	325	2.0	12.0	0.46	39.0	7.1	7.1
Discovery	0-0.3	2.93	12	82	55	126	147	F(F)	1.0005	0.75	1.27	6.7	0.6	450	2.0	10.5	0.45	35.0	6.5	5.5
Valdivia	0-0.3	2.76	5	96	71	80	113	F(F)	1.0003	0.25	0.42	2.2	0.3	300	1.0	24.0	0.37	18.5	10.0	1.8

C_c*: determined for σ' = 1-10 kPa; C_c** : determined for σ' = 10-100 kPa; η-exponent = 0.33 for all sediments.

(Superconducting Quantum Interference Device Vibrating Sample Magnetometer). Fig. 8b shows the magnetization curves for the different sediment samples. The Wando specimen shows a linear magnetic response typical of paramagnetic sediments. The Discovery and Valdivia samples show a slightly sigmoidal curve. The Atlantis II sediments exhibit non-linear sigmoidal-shaped curves characteristic of a material with ferromagnetic components, yet hysteresis curves do not display remnant magnetization in agreement with the small μm-to-nm-sized ferromagnetic particles dispersed throughout the sediment (e.g., Hunt et al., 1995). The relative magnetic permeabilities range from μ_r = 1.0003 (Valdivia sample) to μ_r = 1.0056 (Atlantis II sample - Table 3). Higher μ_r values positively correlate with Fe content (Klein and Santamarina, 2000); however, there is no clear correlation between Fe content and metals of economic interest such as Ag, Cu, Pb and Zn. For reference, common, non-Fe minerals, such as calcite or anhydrite are diamagnetic (μ_r = 0.99994); on the other hand, sulfides, Fe-rich clays and carbonates, Fe-oxides and oxyhydroxides have relative magnetic permeabilities that range from μ_r = 1.0004 for chalcopyrite to μ_r = 6.7 for magnetite (Hunt et al., 1995).

3.4. Geomechanical properties

Oedometer tests. To assess self-compaction behavior during burial, we performed consolidation tests in oedometer cells under zero-lateral-strain conditions using remolded destructured specimens at their in-situ pore fluid and water content; thus, test results provide the “inherent characteristics” of sediments considering brine effects but without their fabric and any possible early diagenetic effects (see also Burland, 1990; Ballas et al., 2018; Yukselen-Aksoy et al., 2008). Specimens were saturated under low vacuum for 12 h prior to testing. The cell remained flooded with a NaCl solution of the same concentration as the in-situ pore fluid to avoid osmotic effects and drying induced suction during the test. We started with very small load increments and reached a final vertical effective stress σ_z' ≈ 1 MPa to capture asymptotic void ratios at low and high effective stress. Results in Fig. 9 show the distinct stress-volume trends for sediments found in the various deeps. The Atlantis II deep sediments exhibit uncharacteristically high compressibility in comparison to sediments from the other deeps in the Red Sea and marine sediments in general (trends in Fig. 9 represent the lower and upper response). The Discovery and Wando deep sediments also show high compressibility. The Valdivia Deep accumulations exhibit low compressibility, similarly to ‘normal’ deep-water Red Sea deposits. These trends highlight the positive correlation between initial void ratio, compressibility, plasticity and specific surface.

We use an asymptotically correct exponential compaction model to capture the void ratio e_z evolution with vertical effective stress σ_z' [kPa] in terms of the asymptotic void ratios e_L at low and e_H high effective stresses (Chong and Santamarina, 2016),

$$e_z = e_H + (e_L - e_H) \exp \left[- \left(\frac{\sigma_z'}{\sigma_c'} \right)^\eta \right] \quad (1)$$

where σ_c' [kPa] is the characteristic effective stress and the η-exponent captures the void ratio sensitivity to effective stress; fitted parameters are summarized in Table 3. The table includes the compression index C_c = (e₁-e₂)/log(σ_{z2}'/σ_{z1}') which is the local slope of the sediment compaction trend between two vertical effective stress levels of interest, σ_{z1}' and σ_{z2}'. In all cases, the compression index for the σ_{z1}' = 10 kPa to σ_{z2}' = 100 kPa effective stress range correlates with the void ratio at 1 kPa in agreement with trends observed for soils worldwide (data in Table 3). Remolded specimens -tested here- provide lower bound estimates of the in-situ compressibility (Burland, 1990).

Small-strain shear wave velocity measurements. Bender elements housed in the upper and lower oedometer caps were used to measure shear wave velocities V_s [m.s⁻¹] at the end of each stress increment. High volume contraction and specimen shortening prevented V_s

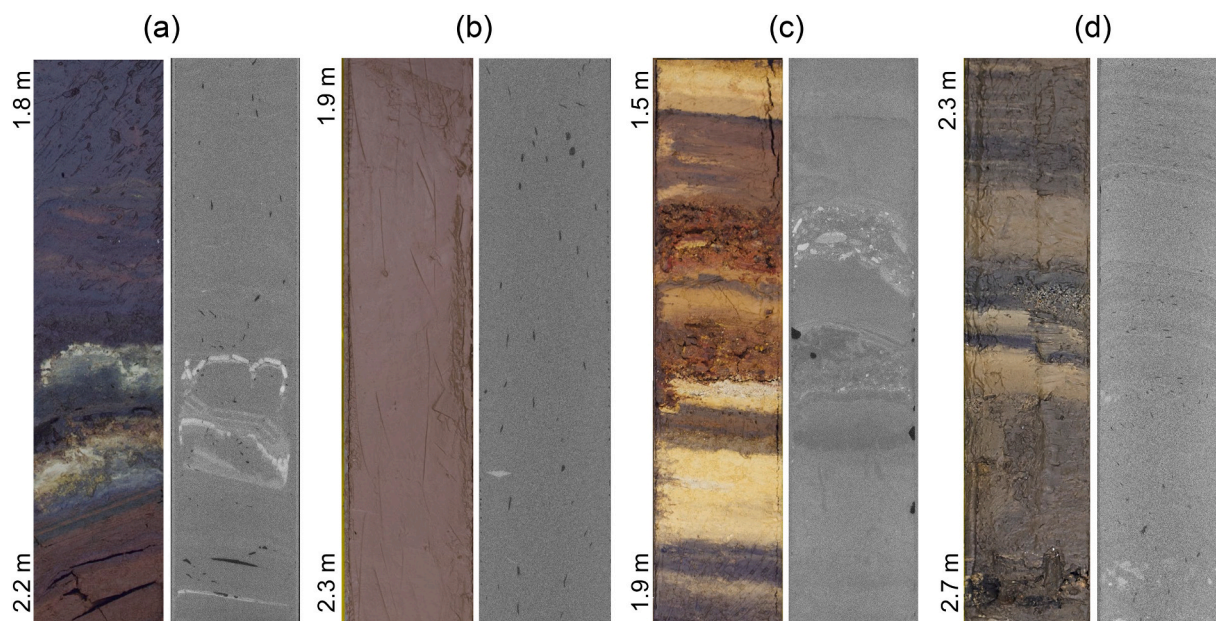


Fig. 2. Slices of 3D X-Ray tomograms and pictures of split cores. (a) Atlantis II deep - North basin, (b) Discovery deep, (c) Wando deep, (d) Valdivia deep. Depths: from the top of the gravity core.

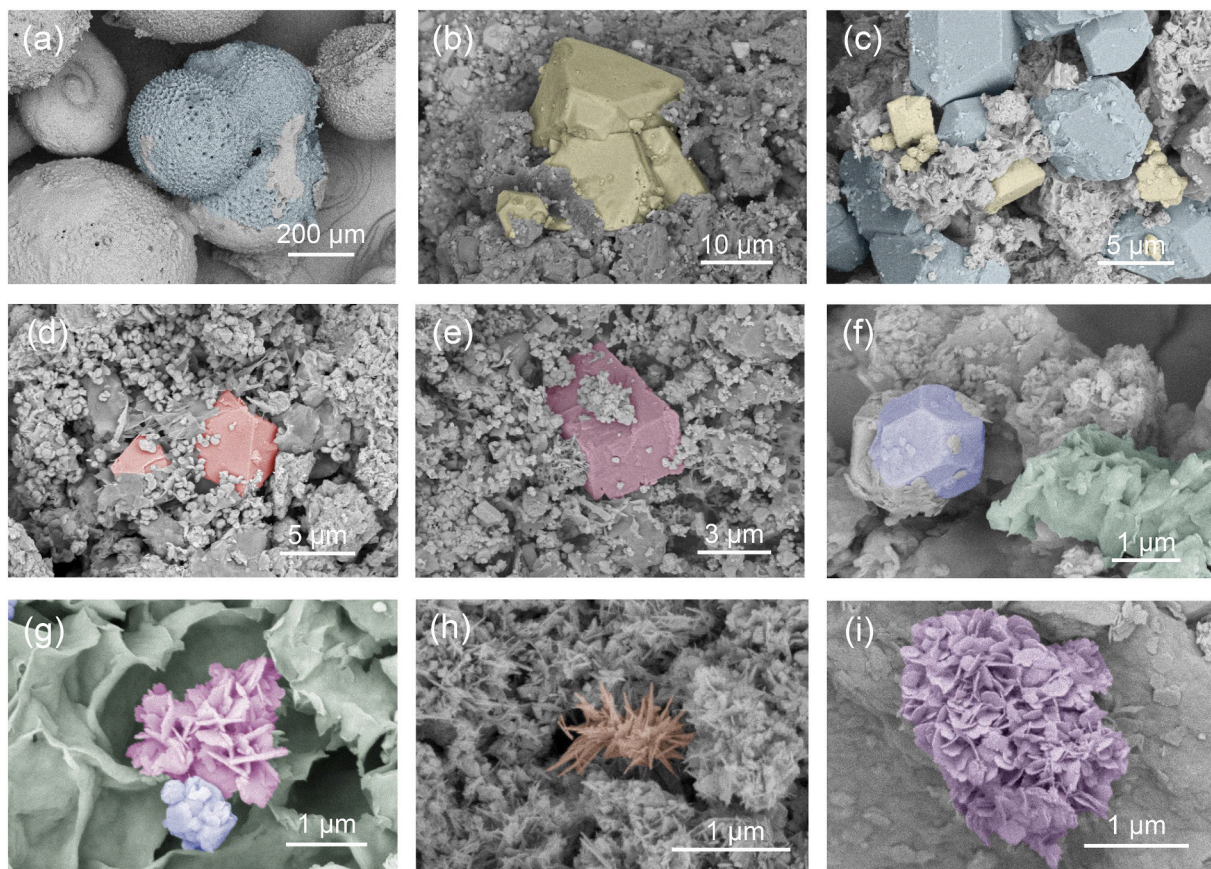


Fig. 3. Scanning electron microscopy images. Atlantis II deep: (a) biogenic carbonate grains with some chemical alteration (foraminifera), (b) euhedral sphalerite crystals embedded in a clay mineral matrix, (c) anhydrite and sphalerite crystals, (d) Fe-oxides, (e) Fe-rich hydrothermal carbonates, (f) sulfide and clay mineral, (g) clay minerals, (h) Fe-oxyhydroxides, (i) clay minerals.

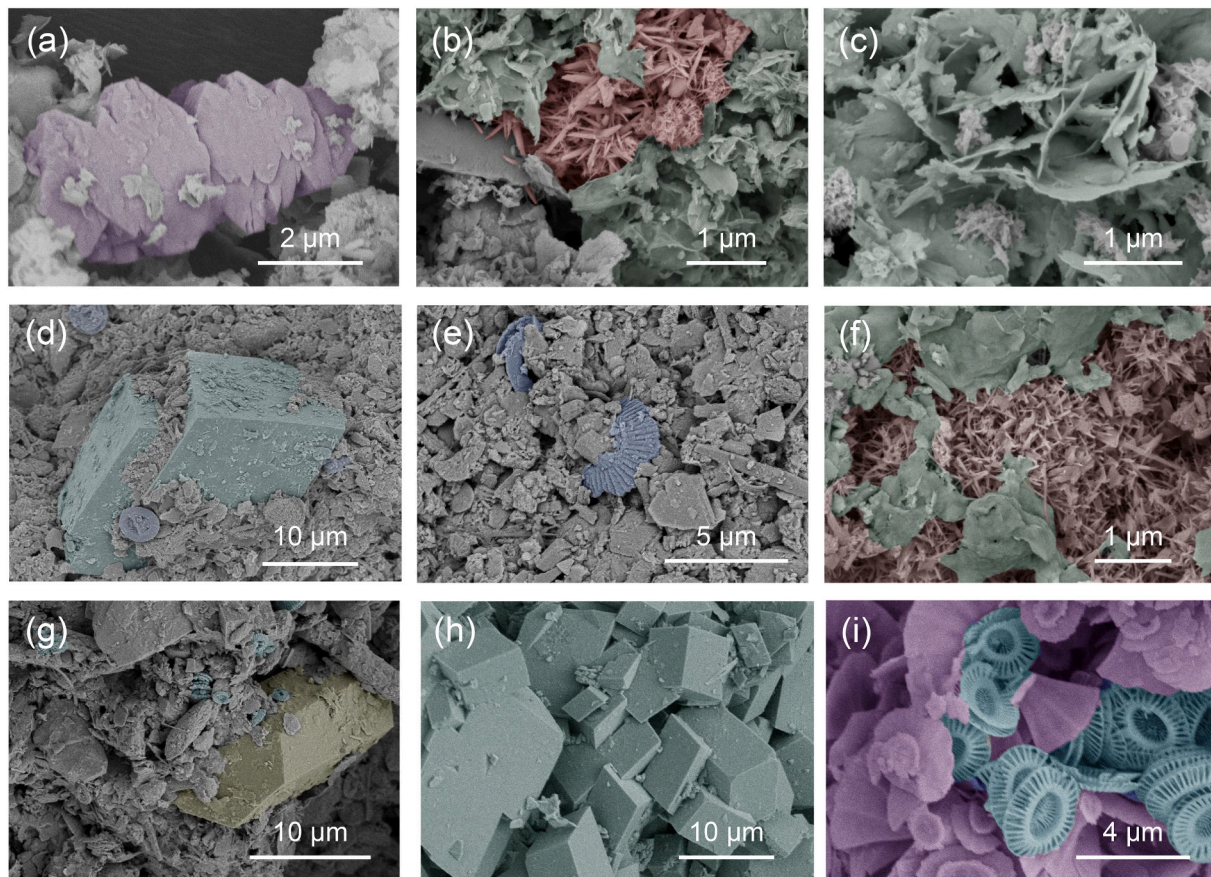


Fig. 4. Scanning electron microscopy images. Wando deep: (a) Mn-oxides, (b) oxides and clay minerals, (c) clay minerals with ‘card-castle’ open fabric. Discovery deep: (d) euhedral dolomite crystal, (e) biogenic carbonate grains (coccoliths), (f) oxides and clay minerals. Valdivia deep: (g) quartz crystal and carbonate biogenic grains, (h) euhedral dolomite crystals, (i) biogenic carbonate grains (coccoliths).

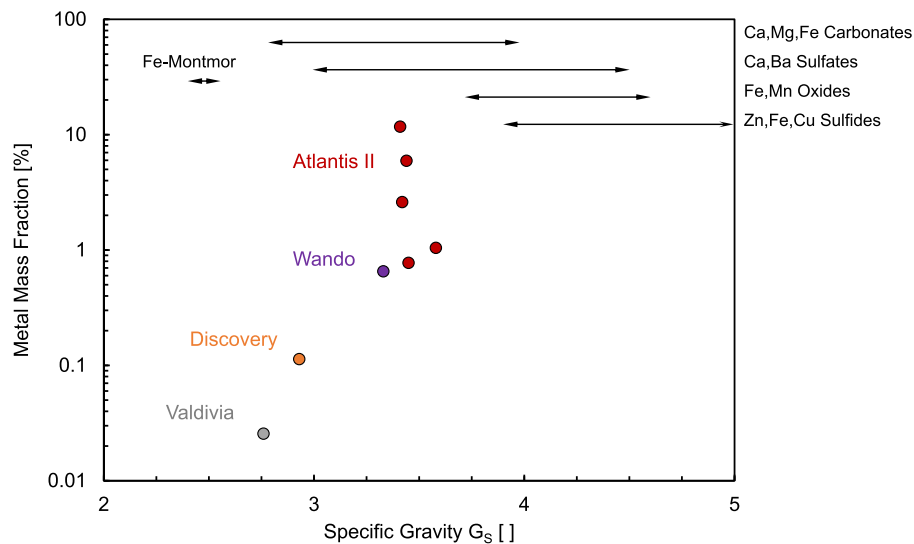


Fig. 5. Metal mass fraction and specific gravity. Metal mass fraction includes Ag, Co, Cu, Pb and Zn (corrected for NaCl concentration). Specific gravity measured for the total sediment, consequently, higher specific gravity correlates with higher metal content. Values of specific surface for pure minerals shown for reference.

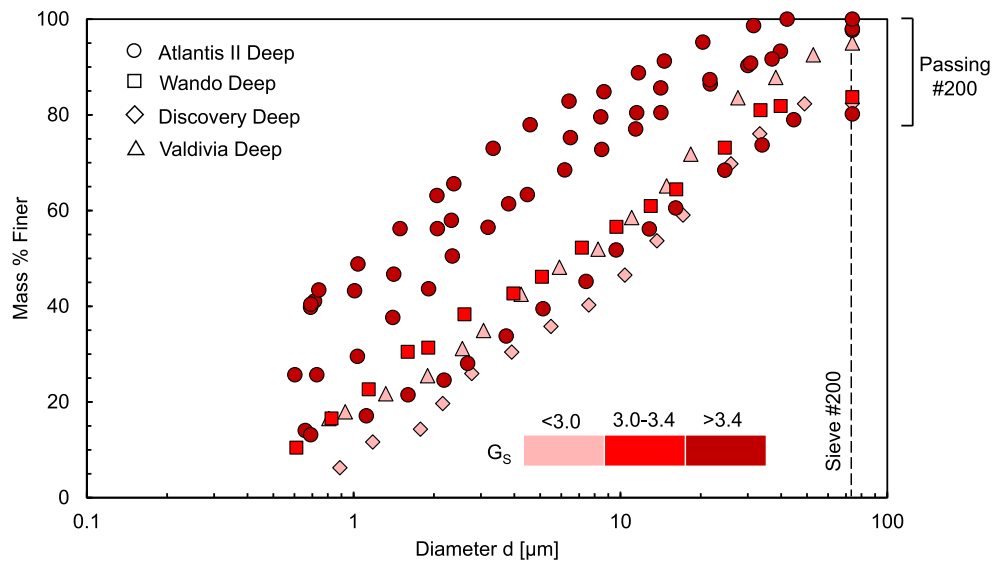


Fig. 6. Grain size distribution. Sediment samples from the Atlantis II, Discovery, Wando and Valdivia deeps. Results obtained using the hydrometer method with dispersant. Data points are color-coded according to the specific gravity measured for the sediment.

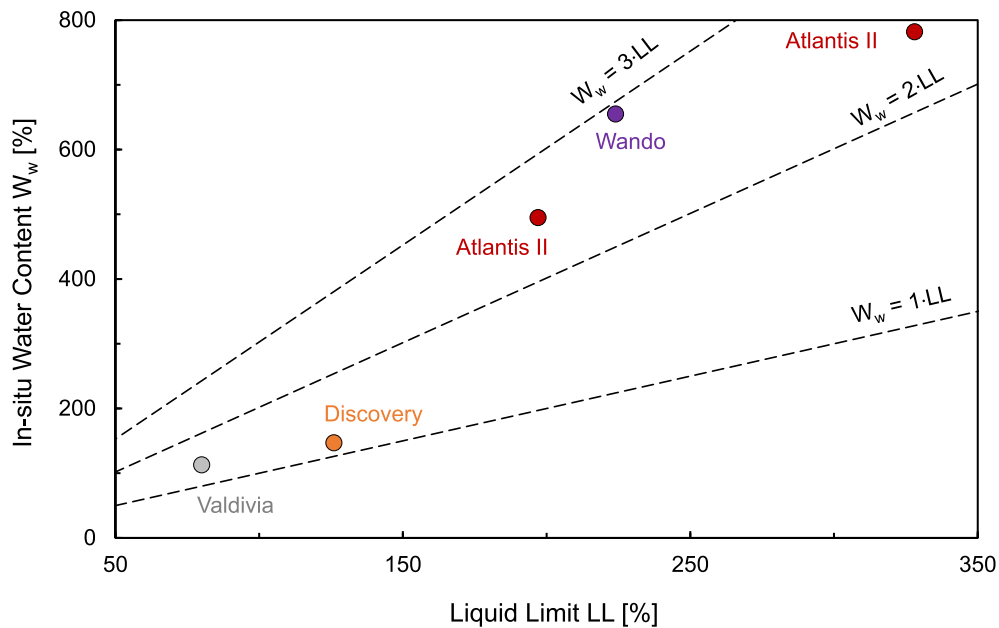


Fig. 7. In-situ water content W_w versus liquid limit LL. Shallow sediments from the Wando, Atlantis, Discovery and Valdivia deeps. Values are corrected for salt precipitation during drying. Liquid limits measured with the in-situ pore fluid.

measurements at vertical stresses above $\sigma'_z > 40$ kPa.

Fig. 10a shows typical signal cascades and Fig. 10b the computed velocities gathered during loading and unloading. Shear wave velocities measured at the end of each load increment follow the characteristic Hertzian-type power equation common to granular materials when the stress levels exceed $\sigma'_z > 10$ kPa (Cha et al., 2014). At low effective stress $\sigma'_z < 10$ kPa, the measured shear wave velocities reflect electrical particle-particle interactions. Therefore, we adopt a modified power model to consider the effects of both electrical and skeletal forces at low effective stress (Sridharan and Rao, 1973; Santamarina et al., 2002),

$$V_s = \alpha \left(\frac{\sigma'_m + \sigma'_A}{1 \text{ kPa}} \right)^\beta \tag{2}$$

where σ'_A is the equivalent effective stress that results from van der Waals attraction between particles, σ'_m is the mean effective stress, and α -factor [$\text{m}\cdot\text{s}^{-1}$] and β -exponent are model parameters. Results show that the equivalent effective stress for electrical interaction ranges between $\sigma'_A = 1$ and $\sigma'_A = 3.5$ kPa.

Compressibility and small strain stiffness. Data collected for sediments worldwide show that more plastic sediments pack in a looser state (higher

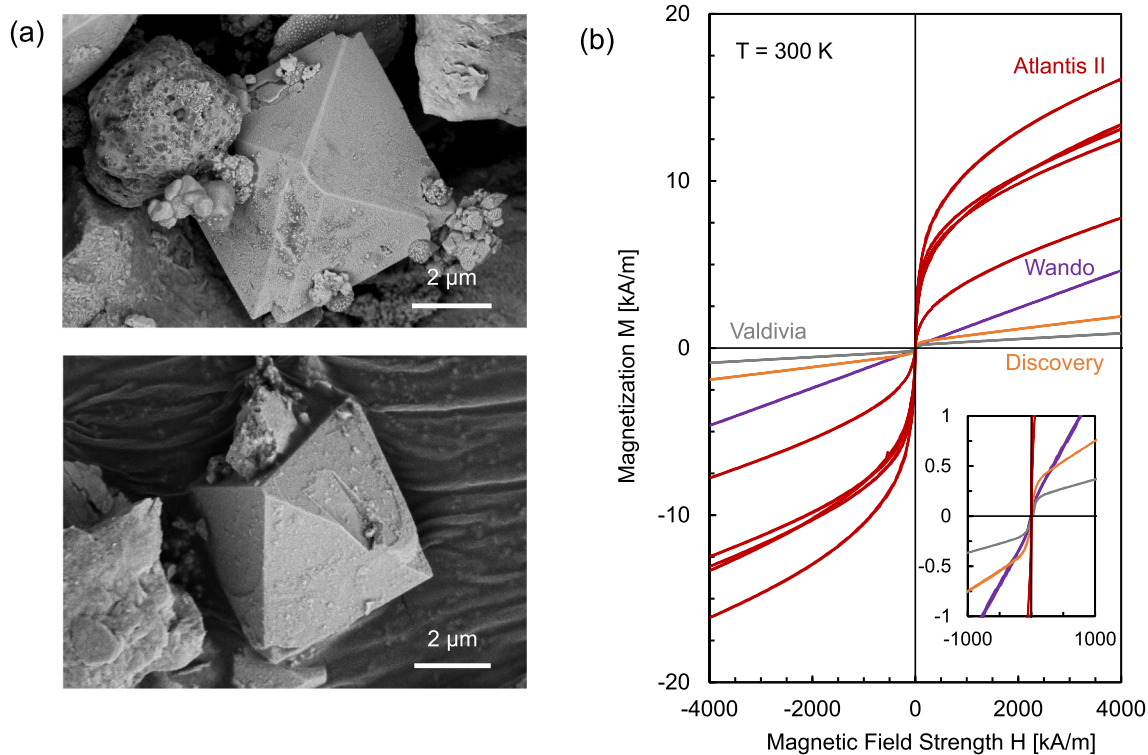


Fig. 8. Magnetic properties. (a) Scanning electron microscope images of magnetically separated particles (magnetite crystals in Atlantis II sediment). (b) Magnetic response M versus magnetic field strength H measured at 300 K (27 °C). The inset shows a close-up for low magnetic field strengths.

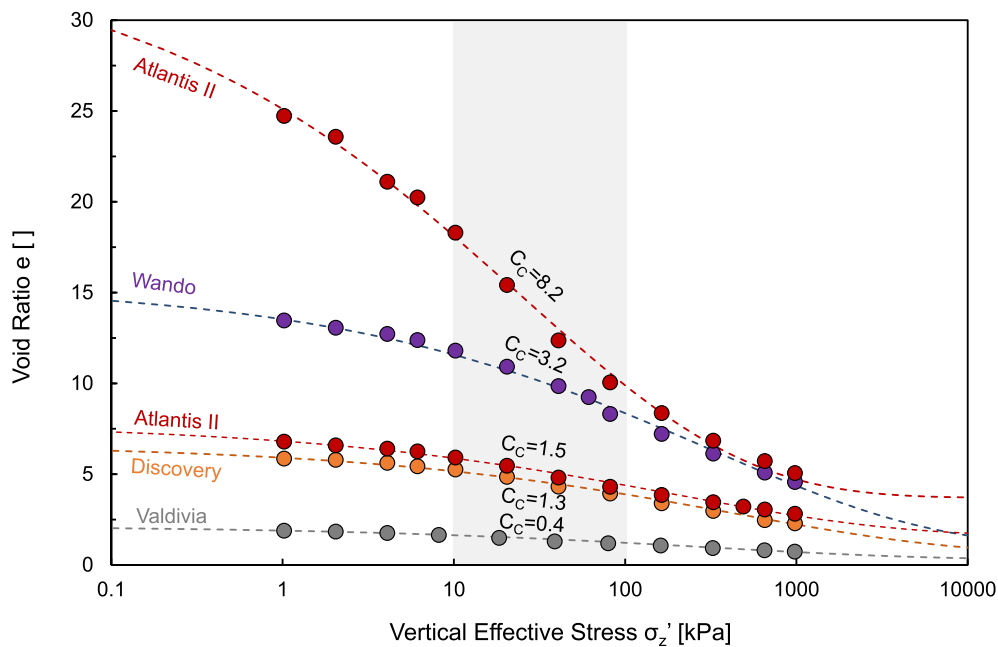


Fig. 9. Consolidation and void ratio reduction as a function of effective stress. Compressibility curves for Atlantis II (upper and lower bounds), Wando, Discovery and Valdivia deep sediments. Filled markers: measurements. Dotted lines: fitted exponential compaction model. Sediment compression index C_c defined between $\sigma'_z = 10$ kPa and $\sigma'_z = 100$ kPa (gray area). Inferred material parameters in Table 3.

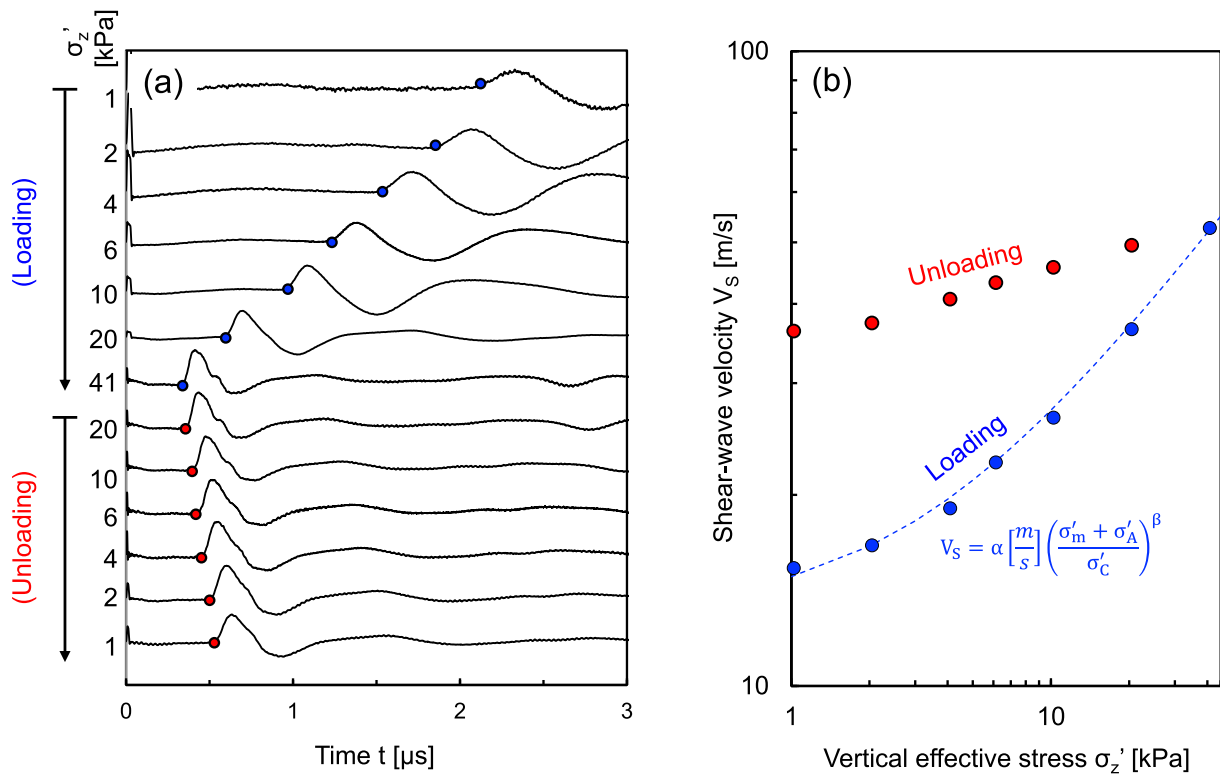


Fig. 10. Shear-wave velocity as a function of effective stress. (a) Typical shear wave signal cascade for loading and unloading paths (Atlantis II deep sediment). (b) Shear-wave velocities V_s [$m \cdot s^{-1}$] measured at the end of each load increment follow a modified power model; the equivalent effective stress σ'_A captures the effects of electrical interparticle forces (Sridharan and Rao, 1973; Santamarina et al., 2001).

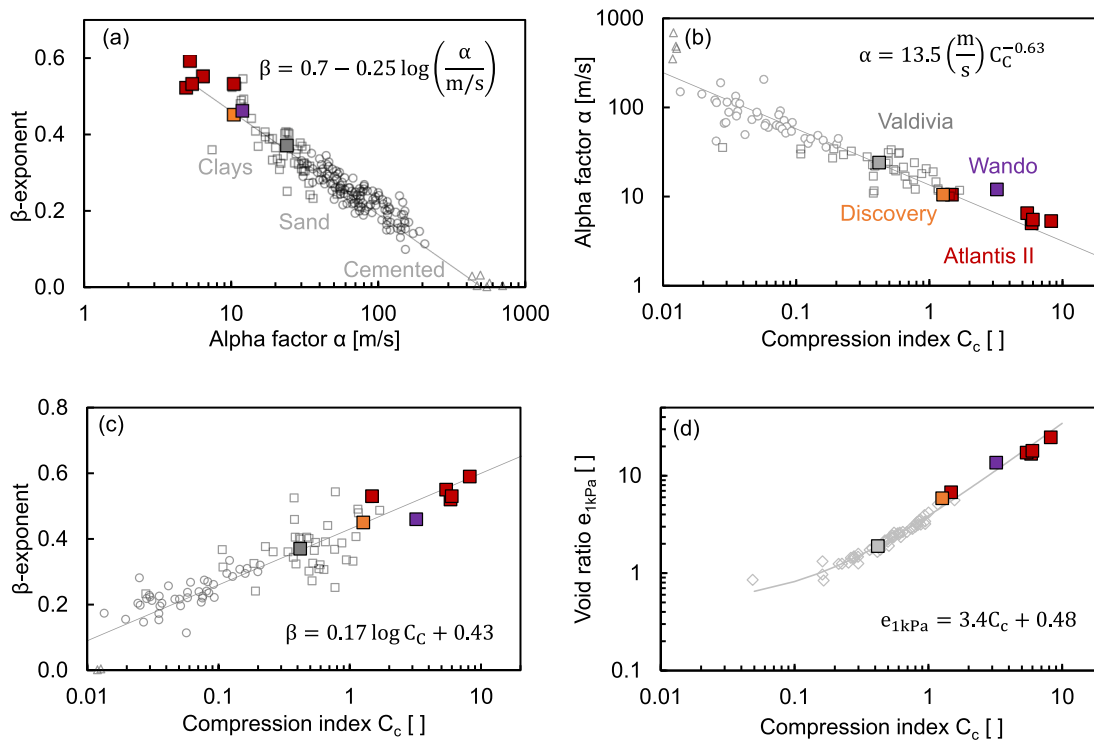


Fig. 11. Relationship between small-strain parameters, void ratio and compressibility. A low α -factor i.e., shear wave velocity at 1 kPa, corresponds to a high β -exponent, i.e., stress sensitivity (a). In fact, both the α -factor and β -exponent are intimately related to compressibility (b&c). Furthermore, looser specimens at 1 kPa stress exhibit higher compressibility (d) where the compression index C_c is calculated between $\sigma'_z = 10$ kPa and $\sigma'_z = 100$ kPa. Filled markers correspond to this study. Data sets for worldwide sediments and trends from Cha et al., 2014 and Chong and Santamarina, 2016. Sediments from Atlantis II, Wando, Discovery and Valdivia deeps align with general soil trends but exhibit extreme characteristics.

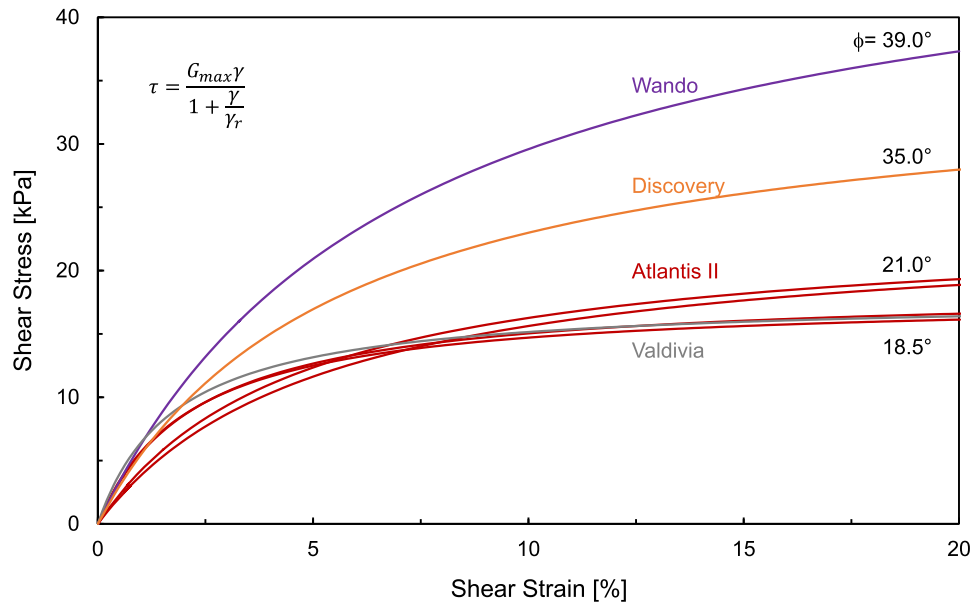


Fig. 12. Shear stress vs. shear strain. Drained simple shear tests conducted with a vertical effective stress $\sigma'_z = 50$ kPa. For clarity, we show the fitted hyperbolic model (Raw data in Supplementary Information).

void ratio e_{1kPa} at 1 kPa), are more compressible (higher C_c), have lower shear wave velocity at 1 kPa (lower α -factor), and higher stress sensitivity (higher β -exponent). Sediments in the four Red Sea deeps studied here confirm these trends (Fig. 11a-d); in particular, hydrothermal sediments emerge as extreme sediments compared to onshore and offshore sediments worldwide (Database from Cha et al., 2014 - values computed in a comparable stress range).

Simple shear: frictional strength. Finally, we performed simple shear tests using remolded specimens at the in-situ water content (Shear Trac II DSS, Geocomp). The procedure included the following steps: (1) pre-consolidation to $\sigma'_z \sim 27$ kPa in an oedometer cell to avoid pronounced specimen shortening in the shear box; (2) specimen transfer to the shear box ring and re-loading in two-step increments, first to $\sigma'_z = 27$ kPa and then to $\sigma'_z = 50$ kPa; and (3) application of horizontal shear under constant vertical effective stress $\sigma'_z = 50$ kPa to a maximum shear displacement of 15 mm. The low shear rate of $0.01 \text{ mm}\cdot\text{min}^{-1}$ ensured pore pressure dissipation and drained conditions (ASTM D3080/D3080M-11). Fig. 12 shows shear strain-stress curves fitted with a hyperbolic model (see fitted parameters in Table 3 and the raw data in Supplementary Information). The measured large-strain friction angles (shear strain $\sim 20\%$) range from $\phi = 19^\circ$ for Atlantis II deep sediments to $\phi = 39^\circ$ for Wando deep sediments (Table 3). The high friction angles reflect the compounded effects of high ionic concentration (Di Maio et al., 2015; Yan and Chang, 2015), the non-platy but rotund particle shape of precipitates (as compared to clay minerals), and the presence of biogenic grains. In fact, similar or even higher friction angles have been reported for other high plasticity sediments such as Ariake clays, Mexico City soils, and Ulleung Basin sediments (Skempton and Jones, 1944; Diaz-Rodriguez et al., 1992; Santamarina and Shin, 2009; Lee et al., 2011).

4. Analyses and discussion

4.1. Sediment formation within the brine pool

Hot hydrothermal fluids fill brine pools where they become supersaturated during cooling, triggering crystal nucleation in the water column. Initial growth is diffusion-controlled while Brownian motion maintains the particles in suspension. Eventually, particles begin to fall through the brine layers with terminal Stokes' velocity. Brownian and

Stokes' velocities are comparable for particle sizes $d \approx 1 \mu\text{m}$ (assuming $\rho_p = 2.7 \text{ g}\cdot\text{cm}^{-3}$). Particles of this size remain ~ 2.8 years in suspension as they fall through the 115 m thick Atlantis II lower brine layer. Particles may grow as they fall through the brine column and the Stokes' velocities increase. Let's assume growth by ion accretion encountered along the particle's pathway: the final particle radius r_f is a function of the fall distance h [m], ion concentration c_b [$\text{kg}\cdot\text{m}^{-3}$] and the particle density ρ_p [$\text{kg}\cdot\text{m}^{-3}$] (derivation in Supplementary Information),

$$r_f = \frac{c_b h}{4\rho_p} \quad (3)$$

Particles could reach $r_f \approx 600 \mu\text{m}$ (Fe-rich particle, $\rho_p = 4 \text{ g}\cdot\text{cm}^{-3}$, $h = 115 \text{ m}$, $c_{bFe} = 1.5 \text{ mmol}\cdot\text{L}^{-1} \approx 87 \text{ g}\cdot\text{m}^{-3}$ - concentration from Schmidt et al., 2003). However, the lower brine is depleted of oxygen so Fe-oxyhydroxides grains do not grow during free fall; indeed, SEM images show that Fe-oxyhydroxides grains rarely exceed $10\text{--}20 \mu\text{m}$. Furthermore, other precipitates that formed in upper layers -such as Mn oxyhydroxides- may dissolve as they fall into the anoxic and acidic lower convective layer. This analysis confirms earlier findings reviewed above.

4.2. Implications for deep-sea mining

Sediment properties control future deep-sea exploration strategies, in-situ resource estimation, extraction and separation, and tailings disposal. Properties measured in this study allow us to anticipate some of these challenges.

Sediment porosity - Significance. Sediment compaction trends in Fig. 9 allow us to predict the evolution of the sediment porosity $n = e/(1 + e)$ with depth by invoking force equilibrium,

$$\frac{\partial \sigma'_z}{\partial z} = g \left(\frac{\rho_{min} - \rho_w}{1 + e_z} \right) \quad (4)$$

where ρ_{min} and ρ_w are the mass densities of minerals and water, and $g = 9.8 \text{ m}\cdot\text{s}^{-2}$. The numerical integration of Eq. 4 with the exponential compaction model in Eq. 1 converts the e_z - σ'_z data in Fig. 9 to porosity-depth trends in Fig. 13. Data for sediments in Red Sea deeps are plotted together with a database of seafloor sediments that ranges from sands to high plasticity clays. Valdivia accumulations display a silt-like behavior that is characteristic of background Red Sea sediments; by contrast,

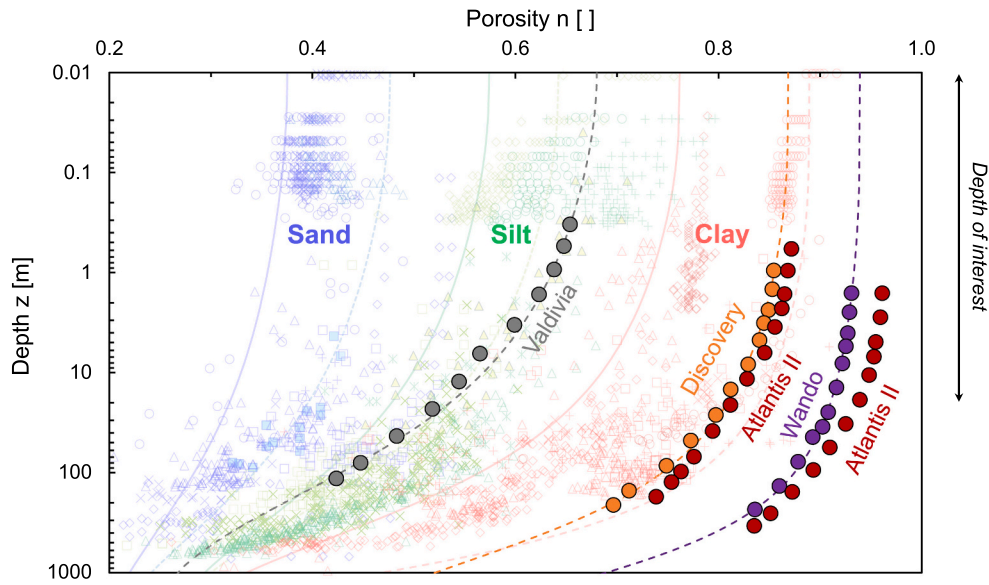


Fig. 13. Porosity versus depth. Data from consolidation tests (Fig. 9) are plotted here against a large database of marine sediments worldwide. Filled markers: sediments in Red Sea deeps (this study); empty markers: database of seafloor sediments (Lyu et al., 2021). Trends: exponential model ($\eta = 0.33$). The depths of interest are the upper ≈ 20 m (average depths values for the Atlantis II deep sediments). Accumulations in the Valdivia deep reflect background Red Sea sedimentation. Hydrothermal genesis, as in Atlantis II and Wando deep sediments, leads to uniquely loose porosity-vs.-depth profiles. (For interpretation of the references to color in this figure legend, the reader is referred to the web version of this article.)

deposits in the Atlantis II, Discovery and Wando deeps exhibit a highly plastic clay-like behavior.

High porosities and low sediment densities (i.e., loose fabric) in the shallow sediments affect mineral estimations. Reported metal concentrations c_{metal} relate the available metal mass M_{metal} [kg] to the sediment mass M_{sed} [kg],

$$c_{metal} = \frac{M_{metal}}{M_{sed}} \quad (5)$$

Then, the total in-situ ore mass in a thin deposit of height H [m] and area A [m²] is (see details in Supplementary Information),

$$M_{metal}^{Reserves} = \int_0^H \frac{M_{metal}}{M_{sed}} \gamma_s \frac{1}{1 + e_z} A dz \quad (6)$$

Consider two deposits of equal metal concentration c_{metal} , sediment unit weight γ_s , depth H and areal extent A ; their relative mineral resources are determined by the compaction trends only.

$$\frac{M_{metal1}}{M_{metal2}} = \frac{\int_0^H \frac{1}{1+e_{1z}} dz}{\int_0^H \frac{1}{1+e_{2z}} dz} \quad (7)$$

If one assumes the density profile of typical pelagic Red Sea sediments in the upper $H = 20$ m, the estimated in-situ metal mass would be ~ 10 times higher than the actual metal mass available in the Atlantis II deep (Fig. 13).

Sampling Challenges. Gravity cores are the most common sampling methods for seafloor sediments. Force balance analysis allow us to estimate the insertion depth z [m] in the quasi-static limit as a function of the corer buoyant self-weight W_B [N] assuming undrained insertion and

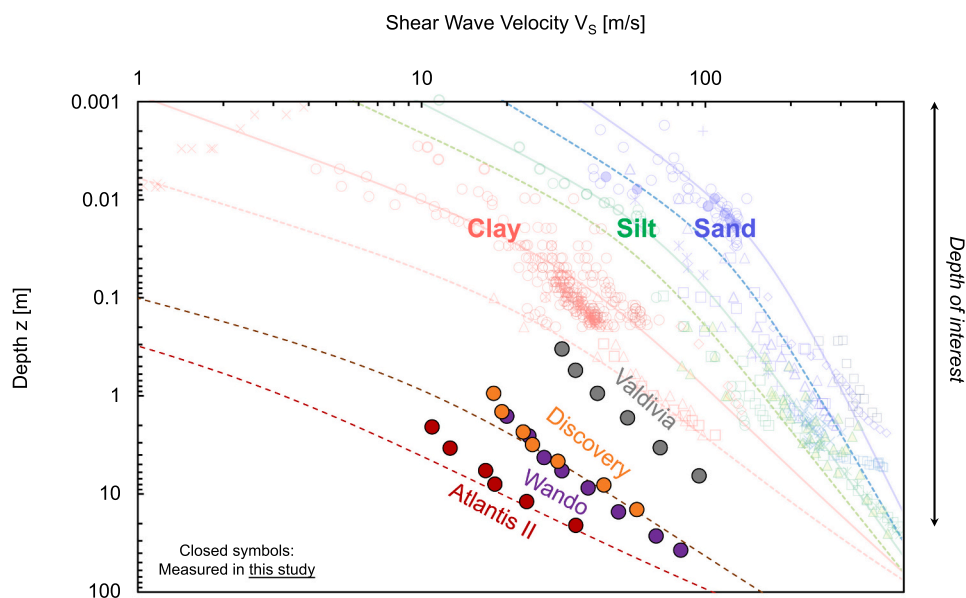


Fig. 14. Shear-wave velocity trends with depth. Hydrothermal sediments exhibit exceptional low velocities. Filled markers: this study. Dotted lines: shear wave power model. Empty symbols: Database for seafloor sediments worldwide from Lyu et al., (2021). The depths of interest are the upper ≈ 20 m (average depth of Atlantis II deep sediments).

the sediment undrained shear strength S_U [kPa] (see details in Supplementary Information). If the corer plugs at the tip, the final insertion depth is reached when the shear resistance mobilized along the corer external wall and the bearing tip resistance equal the corer buoyant weight,

$$W_b = 2\pi r \left(0.2\sigma'_{zav} \right) + 15\pi r^2 \left(0.2\sigma'_{ztip} \right) \quad (8)$$

where r [m] is the corer radius, and σ'_{zav} [kPa] and σ'_{ztip} [kPa] are the average effective stress along the gravity core and the effective stress at the corer tip. If the corer does not plug, the undrained shear resistance is mobilized inside and outside the corer walls, and the ultimate insertion can be estimated from,

$$W_b = 4\pi r \left(0.2\sigma'_{zav} \right) \quad (9)$$

Consider a 90 mm diameter gravity corer with a buoyant weight $W_b = 830$ N (100 kg corer). The iterative solution of eqs. 8, 9 and 1 predicts penetration depths as high as $z = 9$ -to-11 m for the lowest density Atlantis II and Wando sediments, and $z = 4$ -to-5 m for the denser Atlantis II and Discovery accumulations (Fig. 13). Therefore, soft shallow sediments flow through the sampler and the upper several meters of the sediment column remain unsampled. Furthermore, these very soft shallow sediments exhibit minimal acoustic impedance contrast with the overlying brines and affect the interpretation of bathymetric and sub-bottom profiler studies (Lyu et al., 2020). Shear wave velocity data gathered in this study in terms of effective stress V_S - σ'_z (e.g., Fig. 10 - Complete dataset in Supplementary Information) are converted to depth profiles in Fig. 14 (same analysis used above - Eqs. 1 & 4) and compared against a database of shear wave velocities gathered for marine sediments worldwide. Once again, these trends confirm the unique characteristics and low stiffness of hydrothermal sediments. P-wave velocities computed from V_S using Biot-Gassman equations enhance the analysis of acoustic measurements in these very soft sediments. Therefore, detailed analysis of remotely determined acoustic impedance measurements can provide important information relevant to sediment type and potential properties.

Separation, processing and extraction. Fine-grained mineral processing confronts particle aggregation, high chemical absorption, low particle momentum and low probability of collision with air bubbles (Sivamohan, 1990). While Red Sea metalliferous sediments are extremely fine, three properties are particularly relevant for separation and enrichment: (1) specific gravities facilitate gravity-based concentration techniques, as ore-bearing minerals can be up to 1.8 times denser than biogenic carbonates (Fig. 5); (2) ferromagnetic characteristics allow for magnetic separation in high magnetic fields albeit with limited efficiency due to small particle size; and (3) high specific surface area and distinct mineral composition may enable selective adsorption of surfactants and particle hydrophobization to support flotation techniques.

Tailing disposal. Mining operations re-suspend fines during extraction and discard most of the mined sediments after separation; therefore, re-sedimentation and tailings disposal gain critical relevance. Fine-grained sediment aggregation is highly susceptible to fluid chemistry, particularly ionic concentrations and pH (Palomino and Santamarina, 2005). The high salinity in Red Sea brine pools favors aggregation into low density flocs; then, convective drag within the stratified layers maintains these aggregates in suspension. Convection in stratified layers resembles a peripheral conveyor belt driven by buoyancy. The convection velocity v_c [$\text{m}\cdot\text{s}^{-1}$] can be estimated as a function of the brine density ρ_b [$\text{kg}\cdot\text{m}^{-3}$], the thermal expansion coefficient α_T [$^{\circ}\text{C}^{-1}$], the thermal jump across the boundary ΔT [$^{\circ}\text{C}$], the convective-belt characteristic thickness λ [m] and the convective layer thickness H_b [m] (see Supplementary Information),

$$v_c = \frac{g \rho_b \lambda}{48 \mu} \frac{\lambda}{H_b} \alpha_T \Delta T \quad (10)$$

where $g = 9.8 \text{ m}\cdot\text{s}^{-2}$ and μ [Pa.s] is the dynamic viscosity. Let's adopt a belt thickness equal to 1/3 the transition layer thickness. Then, the estimated convection velocities within the lower layer in the Atlantis II brine pool are in the order of $v_c \approx 10 \text{ cm}\cdot\text{s}^{-1}$. Fined-grained particles and light density flocs with low Stokes' velocity $v_{St} < v_c$ will have long residency times in convective stratified layers. For reference, particles smaller than $d \approx 0.3 \text{ mm}$ ($\rho_p = 2.7 \text{ g}\cdot\text{cm}^{-3}$, $\rho_b = 1.19 \text{ g}\cdot\text{cm}^{-3}$) have terminal velocities below $10 \text{ cm}\cdot\text{s}^{-1}$. Clearly, the environmental impact and implications of deep-sea mining and submarine tailings disposal in the Red Sea brine bodies requires careful analysis.

5. Conclusions

Sedimentary columns at the various deeps within the central Red Sea reflect distinct combinations between slow-rate background sedimentation (dominant in the Valdivia deep) and hydrothermal metalliferous sediment formation that nucleate and grow within the overlying brine pools (prevalent at Atlantis II and Wando deeps; sediments in the Discovery deep have a mixed origin). Marked layering and compositional changes record pronounced fluctuations in the formation environments, including periods of high hydrothermal activity in the last few thousand years.

Sediments within the four deeps are made of fine-grained silt and clay-size particles. Background sedimentation consist of biogenic carbonates and detrital silicate particles. Layers formed as a result of hydrothermal activity contain sulfides, sulfates, clays, Fe-Mn oxides, and carbonates.

Sediments of hydrothermal origin exhibit extreme characteristics when compared to onshore and offshore sediments worldwide. Their shear wave velocity is highly sensitivity to effective stress, i.e., burial depth. Velocity-stress trends highlight the effect of inter-particle electrical attraction at low effective stress (the equivalent effective stress due to van der Waals attraction is between 1.5 and 3.5 kPa). High salinity, the rotund shape of precipitates and the presence of biogenic particles explain the high measured friction angles, which can exceed $\phi = 35^{\circ}$.

Hydrothermal sediments have very high specific surface area, their in-situ water content remains above the liquid limit within the depth of interest, and their uncharacteristically high maximum void ratio and compressibility result in very low sediment density profiles that are very different from background Red Sea sediments. Their low density has a strong effect on remote acoustic characterization, sampling strategies and resource estimation. Consequently, previous estimations of sediment thickness and metal mass should be carefully revisited.

Sediments in the Atlantis II offer the highest mining potential followed by the Wando deep. The smaller particles tend to have higher specific gravity, define the metalliferous content and exhibit magnetic permeabilities above background mineral paramagnetism. Elevated specific gravity and ferromagnetic characteristics can guide the selection and design of separation and enrichment processes.

Fines aggregate in Red Sea brines to form low density flocs with Stokes' terminal velocity lower than convection velocities within stratified layers. Therefore, fines and aggregates may experience extended residency times in convective brine pools. This observation gains relevance for environmental analyses of seafloor mining operations and tailings disposal.

Author statement

M. Clara Modenesi & J. Carlos Santamarina worked together on conceptualization, test protocols, analyses and manuscript preparation. M. Clara Modenesi run all test sequences.

Declaration of Competing Interest

The authors declare that they have no known competing financial

interests or personal relationships that could have appeared to influence the work reported in this paper.

Acknowledgements

Support for this research was provided by the KAUST endowment at King Abdullah University of Science and Technology. The science teams led by Marco Terzariol and the crew of RV Thuwal facilitated all field operations. Marisol Salva helped with characterization protocols. Gabrielle E. Abelskamp edited the manuscript.

Appendix A. Supplementary data

Supplementary data to this article can be found online at <https://doi.org/10.1016/j.enggeo.2022.106720>.

References

- Anschutz, P., Blanc, G., 1995a. Diagenetic evolution of the DOP facies from the Atlantis-II-deep (Red Sea)-evidence of early hydrothermal activity. *Oceanol. Acta* 18 (1), 105–112.
- Anschutz, P., Blanc, G., 1995b. Geochemical dynamics of the Atlantis II deep (Red Sea): silica behavior. *Mar. Geol.* 128 (1–2), 25–36.
- ASTM International, 2014. D854-14 Standard Test Methods for specific Gravity of Soil Solids by Water Pycnometer. ASTM International, West Conshohocken, PA. <https://doi.org/10.1520/D0854-14>.
- ASTM International, 2017. D7928-17 Standard Test Method for Particle-size distribution (Gradation) of Fine-Grained Soils using the Sedimentation (Hydrometer) analysis. ASTM International, West Conshohocken, PA. <https://doi.org/10.1520/D7928-17>.
- Augustin, N., Devey, C.W., Van der Zwan, F.M., Feldens, P., Tominaga, M., Bantan, R.A., Kwasnitschka, T., 2014. The rifting to spreading transition in the Red Sea. *Earth Planet. Sci. Lett.* 395, 217–230.
- Augustin, N., van der Zwan, F.M., Devey, C.W., Ligi, M., Kwasnitschka, T., Feldens, P., Bantan, R.A., Basaham, A.S., 2016. Geomorphology of the Central Red Sea Rift: determining spreading processes. *Geomorphology* 274, 162–179.
- Bäcker, H., Richter, H., 1973. Die rezente hydrothermal-sedimentäre Lagerstätte Atlantis-II-Tief im Roten Meer. *Geol. Rundsch.* 62 (3), 697–737.
- Backer, H., Schoell, M., 1972. New deeps with brines and metalliferous sediments in the Red Sea. *Nat. Phys. Sci.* 240 (103), 153–158.
- Ballas, G., Garziglia, S., Sultan, N., Pelleter, E., Toucanne, S., Marsset, T., Riboulot, V., Ker, S., 2018. Influence of early diagenesis on geotechnical properties of clay sediments (Romania, Black Sea). *Eng. Geol.* 240, 175–188.
- Bignell, R.D., Cronan, D.S., Tooms, J.S., 1976. Red Sea metalliferous brine precipitates. In: *Special paper - Geological Association of Canada*, 14, pp. 147–184.
- Bischoff, J.L., 1969. Red Sea geothermal brine deposits: Their mineralogy, chemistry, and genesis. In: *Hot Brines and Recent Heavy Metal Deposits in the Red Sea*. Springer, Berlin, Heidelberg, pp. 368–401.
- Blouin, A., Sultan, N., Callot, J.P., Imbert, P., 2019. Sediment damage caused by gas exsolution: a key mechanism for mud volcano formation. *Eng. Geol.* 263, 105313.
- BSI, 1990. BS 1377-2: Methods of Test for Soils for Civil Engineering Purposes (classification tests). British Standard Institution, London, UK.
- Burland, J.B., 1990. On the compressibility and shear strength of natural clays. *Géotechnique* 40 (3), 329–378.
- Butuzova, G.Y., Drits, V.A., Morozov, A.A., Gorskov, A.I., 1990. Processes of Formation of Iron–Manganese Oxyhydroxides in the Atlantis-II and Thetis Deeps of the Red Sea. In: *Sediment-Hosted Mineral Deposits: Proceedings of a Symposium Held in Beijing, People's Republic of China, 30 July–4 August 1988*. Blackwell Publishing Ltd., Oxford, UK, pp. 57–72.
- Cha, M., Santamarina, J.C., Kim, H.S., Cho, G.C., 2014. Small-strain stiffness, shear-wave velocity, and soil compressibility. *J. Geotech. Geoenviron.* 140 (10), 06014011.
- Charnock, H., 1964. Anomalous bottom water in the Red Sea. *Nature* 203 (4945), 591.
- Chong, S.H., Santamarina, J.C., 2016. Soil compressibility models for a wide stress range. *J. Geotech. Geoenviron.* 142 (6), 06016003.
- Coleman, R.G., 1993. *Geological Evolution of the Red Sea*. Oxford Monographs on Geology and Geophysics. Oxford University Press, New York, p. 186.
- Dai, S., Santamarina, J.C., 2014. Sampling disturbance in hydrate-bearing sediment pressure cores: NGHP-01 expedition, Krishna–Godavari Basin example. *Mar. Pet. Geol.* 58, 178–186.
- Degens, E.T., Ross, D.A., 1969. Hot Brines and Recent Heavy Metal Deposits in the Red Sea A Geochemical and Geophysical Account.
- Di Maio, C., Scaringi, G., Vassallo, R., 2015. Residual strength and creep behaviour on the slip surface of specimens of a landslide in marine origin clay shales: influence of pore fluid composition. *Landslides* 12 (4), 657–667.
- Diaz-Rodriguez, J.A., Leroueil, S., Aleman, J.D., 1992. Yielding of Mexico City clay and other natural clays. *J. Geotech. Eng.* 118 (7), 981–995.
- Engelbrecht, J., Stenichkov, G.L., Prakash, P.J., Lersch, T., Anisimov, A., Shevchenko, I., 2017. Physical and chemical properties of deposited airborne particulates over the Arabian Red Sea coastal plain. *Atmos. Chem. Phys.* 17 (18), 11467–11490.
- Gevirtz, J.L., Friedman, G.M., 1966. Deep-sea carbonate sediments of the Red Sea and their implications on marine lithification. *J. Sediment. Res.* 36 (1), 143–151.
- Guney, M., Al-Marhoun, M.A., Nawab, Z.A., 1988. Metalliferous sub-marine sediments of the Atlantis-II-Deep, Red Sea. *Canadian Institute of Mining and Metallurgy Bulletin* 81, 33–39.
- Hackett, J.P., Bischoff, J.L., 1973. New data on the stratigraphy, extent, and geologic history of the Red Sea geothermal deposits. *Econ. Geol.* 68 (4), 553–564.
- Hartmann, M., 1985. Atlantis-II deep geothermal brine system. Chemical processes between hydrothermal brines and Red Sea deep water. *Mar. Geol.* 64 (1–2), 157–177.
- Hunt, C.P., Moskowitz, B.M., Banerjee, S.K., 1995. Magnetic properties of rocks and minerals. In: *Rock Physics and Phase Relations: A Handbook of Physical Constants*, 3, pp. 189–204.
- Izzeldin, A.Y., 1987. Seismic, gravity and magnetic surveys in the central part of the Red Sea: their interpretation and implications for the structure and evolution of the Red Sea. *Tectonophysics* 143 (4), 269–306.
- Jang, J., Santamarina, J.C., 2016. Fines classification based on sensitivity to pore-fluid chemistry. *J. Geotech. Geoenviron.* 142 (4), 06015018.
- Klein, K., Santamarina, J.C., 2000. Ferromagnetic inclusions in geomaterials: Implications. *J. Geotech. Geoenviron.* 126 (2), 167–179.
- Laurila, T.E., Hannington, M.D., Petersen, S., Garbe-Schönberg, D., 2014. Trace metal distribution in the Atlantis II deep (Red Sea) sediments. *Chem. Geol.* 386, 80–100.
- Laurila, T.E., Hannington, M.D., Leybourne, M., Petersen, S., Devey, C.W., Garbe-Schönberg, D., 2015. New insights into the mineralogy of the Atlantis II deep metalliferous sediments, Red Sea. *Geochem. Geophys. Geosyst.* 16 (12), 4449–4478.
- Lee, C., Yun, T.S., Lee, J.S., Bahk, J.J., Santamarina, J.C., 2011. Geotechnical Characterization of Marine Sediments in the Ullung Basin, East Sea. *Engineering Geology* 117, 151–158.
- Lyu, C., Park, J., Carlos Santamarina, J., 2020. Depth-dependent seabed properties: geoaoustic assessment. *J. Geotech. Geoenviron.* 147 (1), 04020151.
- Mavko, G., Mukerji, T., Dvorkin, J., 2009. *The Rock Physics Handbook: Tools for Seismic Analysis of Porous Media*. Cambridge University Press.
- Miller, A.R., 1964. Highest salinity in the world ocean. *Nature* 203 (4945), 590–591.
- Miller, A.R., Densmore, C.D., Degens, E.T., Hathaway, J.C., Manheim, F.T., McFarlin, P. F., Pocklington, R., Jokela, A., 1966. Hot brines and recent iron deposits in deeps of the Red Sea. *Geochim. Cosmochim. Acta* 30 (3), 341–359.
- Mitchell, N.C., Ligi, M., Ferrante, V., Bonatti, E., Rutter, E., 2010. Submarine salt flows in the Central Red Sea. *Bulletin* 122 (5–6), 701–713.
- Mustafa, Z., Amann, H.M., 1980. The Red Sea pre-pilot mining test 1979. In: *Offshore Technology Conference*. Offshore Technology Conference.
- Orszag-Sperber, F., Harwood, G., Kendall, A., Purser, B.H., 1998. A review of the evaporites of the Red Sea-Gulf of Suez rift. *Sedimentation and Tectonics in Rift Basins Red Sea-Gulf of Aden* 409–426.
- Palomino, A., Santamarina, J.C., 2005. Fabric Map for Kaolinite (Single Mineral): Effects of pH and Ionic Concentration on Behavior. *Clay Clay Miner.* 53 (3), 211–223.
- Park, J., Santamarina, J.C., 2017. Revised soil classification system for coarse-fine mixtures. *J. Geotech. Geoenviron.* 143 (8), 04017039.
- Pierret, M.C., Clauer, N., Blanc, G., 2000. Influence hydrothermale dans les sédiments de fosses de la mer Rouge par l'étude de quelques éléments traces. *Oceanol. Acta* 23 (7), 783–792.
- Salva Ramirez, M., Santamarina, J.C., 2021. Specific Surface Area by Colorimetry and Image Analysis. *Geotech. Test. J.* 45 (1).
- Santamarina, J.C., Klein, K.A., Fam, M.A., 2001. *Soils and waves*. J. Wiley & Sons, New York.
- Santamarina, J.C., Shin, H., 2009. Friction in granular media. In: *Meso-Scale Shear Physics in Earthquake and Landslide Mechanics*. CRC Press, London, pp. 157–188.
- Santamarina, J.C., Klein, K.A., Wang, Y.H., Prencke, E., 2002. Specific surface: determination and relevance. *Can. Geotech. J.* 39 (1), 233–241.
- Schmidt, M., Botz, R., Faber, E., Schmitt, M., Poggenburg, J., Garbe-Schönberg, D., Stoffers, P., 2003. High-resolution methane profiles across anoxic brine-seawater boundaries in the Atlantis-II, Discovery, and Kebrut Deeps (Red Sea). *Chem. Geol.* 200 (3–4), 359–375.
- Shanks, W.C., Bischoff, J.L., 1980. Geochemistry, sulfur isotope composition, and accumulation rates of Red Sea geothermal deposits. *Econ. Geol.* 75 (3), 445–459.
- Shanks III, W.C., Bischoff, J.L., 1977. Ore transport and deposition in the Red Sea geothermal system: a geochemical model. *Geochim. Cosmochim. Acta* 41 (10), 1507–1519.
- Siam, R., Mustafa, G.A., Sharaf, H., Moustafa, A., Ramadan, A.R., Antunes, A., Bajic, V.B., Stingl, U., Marsis, N.G., Coolen, M.J., Sogin, M., 2012. Unique prokaryotic consortia in geochemically distinct sediments from Red Sea Atlantis II and Discovery deep brine pools. *PLoS One* 7 (8), e42872.
- Sivamohan, R., 1990. The problem of recovering very fine particles in mineral processing—a review. *Int. J. Miner. Process.* 28 (3–4), 247–288.
- Skempton, A.W., Jones, O.T., 1944. Notes on the compressibility of clays. *Q. J. Geol. Soc.* 100 (1–4), 119–135.
- Sridharan, A., Rao, G.V., 1973. Mechanisms controlling volume change of saturated clays and the role of the effective stress concept. *Géotechnique* 23 (3), 359–382.
- Stoffers, P., Ross, D.A., 1974. Sedimentary history of the Red Sea, Initial Reports Deep Sea Drilling Proj, XXIII, pp. 849–865.
- Swallow, J.C., Crease, J., 1965. Hot salty water at the bottom of the Red Sea. *Nature* 205 (4967), 165–166.
- Taitel-Goldman, N., Singer, A., 2001. High-resolution transmission electron microscopy study of newly formed sediments in the Atlantis II deep, Red Sea. *Clays and Clay Minerals* 49 (2), 174–182.
- Taitel-Goldman, N., Singer, A., 2002. Metastable Si-Fe phases in hydrothermal sediments of Atlantis II deep, Red Sea. *Clay Minerals* 37 (2), 235–248.

Turner, J.S., 1969. A physical interpretation of the observations of hot brine layers in the Red Sea. In: *Hot Brines and Recent Heavy Metal Deposits in the Red Sea*. Springer, Berlin, Heidelberg, pp. 164–173.

Yan, W.M., Chang, J., 2015. Effect of pore water salinity on the coefficient of earth pressure at rest and friction angle of three selected fine-grained materials. *Eng. Geol.* 193, 153–157.

Yukselen-Aksoy, Y., Kaya, A., Ören, A.H., 2008. Seawater effect on consistency limits and compressibility characteristics of clays. *Eng. Geol.* 102 (1–2), 54–61.